MECSOL 2022 - Proceedings of the 8th International Symposium on Solid Mechanics
M.L. Bittencourt, J. Labaki, L.C.M. Vieira Jr. and E. Mesquita (Editors), Campinas SP, Brazil, October 17th to 19th, 2022

NUMERICAL STRUCTURAL ANALYSES OF CENTRIFUGAL COMPRESSORS OPERATING WITH CO2 IN A SUPERCRITICAL STATE

D. Z. Lima [1], L. N. de Carvalho [1], D. J. Dezan [1], E. E. Gasparin [2], V. C N. Mattos [2], L. O. Salviano [2], P. E. B. de Mello [3], F. Saltara [4], J. I. Ynagihara, W. G. Ferreira [1].

[1] Federal University of ABC – UFABC - Av. dos Estados, 5001 - Bangú, 09210-580, Santo André/SP, Brazil

[2] UNESP – Ilha Solteira - Av. Brasil Sul, 56 – Centro, 15385-000, Ilha Solteira/SP, Brazil

[3] Centro Universitário FEI - Av. Humberto de Alencar Castelo Branco, 3972-B - Assunção, São Bernardo do Campo/SP

[4] USP - University of São Paulo - Av. Prof. Mello Moraes, 2231 - Cidade Universitária, 05508-080, São Paulo/SP, Brazil

Abstract: Carbon dioxide (CO2) is the main greenhouse gas (GHG), and its presence in the atmosphere has increased from 280 ppm in 1750 to more than 400 ppm in the current years. Therefore, in addition to the direct reduction using new sources of energy, it is necessary to advance toward Carbon Capture, Storage, and Utilization (CCSU) technologies. The research focused on CCSU is expanding knowledge on the use of CO2 in a supercritical state (sCO2). The use of sCO2 as a working fluid enables more compact and efficient equipment in both transportation and power generation cycles. However, their properties have a highly nonlinear behavior near the critical point. But the use of inlet conditions close to this region maximizes the advantages of sCO2, corroborating for new research to be carried out to improve the numerical design models. Regarding the structure, the use of sCO2 as a working fluid provides the construction of more compact structures, reducing the mass of the components as well as the cost of materials. Nevertheless, due to the high specific mass, the aerodynamic loads resulting from the fluid-structure interaction have a larger amplitude. This directly affects the vibration frequencies, modes shape, and static behavior of the impeller. Therefore, careful studies of the structural failure modes and modal analysis to verify resonance are essential to ensure structural integrity and to design components with long service life. In this context, this work focused on static and modal structural analyses in three case studies. The first one was performed with a centrifugal compressor presented in the literature, and the following two with the application in CCSU. Based on the performed analyzes, new geometries for the compressors were proposed. The results showed that for the compressor of the literature and the first stage, the aerodynamic loads did not have a great influence on the static behavior, but for the case of the fourth stage, they were the main source of load and had to be treated in detail.

Keywords: centrifugal compressor, structural analysis, fluid-structural interaction, finite element analysis, optimization.

INTRODUCTION

Carbon dioxide (CO2) is the principal greenhouse gas (GHG), and the emissions over the centuries have increased its presence in the atmosphere from 280 ppm in 1750, to more than 400 ppm in the current years, (Umezawa et al., 2020). Thus, new technologies focused on Carbon Capture, Storage, and Utilization (CCSU) are attracting the interest of companies and governments, (Baena-Moreno et al., 2018; Page et al., 2020).

The research focused on CCSU is expanding knowledge on the use of CO2 in the supercritical state (sCO2), as an alternative to more efficient transport and power generation processes (White et al., 2021). Motivated by the great advantages that the use of sCO2 as a working fluid brings, such as compact structures and highly efficient compression. However, the properties of sCO2 vary highly nonlinearly near the critical point. Making the design of compressors a challenging task since the inlet conditions are usually close to the critical point. Then, works focused on improving the design project are extremely necessary.

The focus of this work will be on the structural design requirements of the impellers aiming for a safe and long service operation (Saravanamuttoo et al., 2017). The analysis of the fluid conditions and CFD (computational fluid dynamics) simulations will not be detailed here. The first case is a validation of the analysis method based on a well-known published air compressor. The second and third cases are compressor impeller geometries currently being designed for CCSU application and operate with CO2 at supercritical conditions.

In each case study, one fundamental concept will be detailed. The first will be the fluid-structural interaction (FSI) and the Campbell diagram for modal analysis. The second will establish the structural design requirements used in the centrifugal compressor projects. And in the last, the backpressure consideration and axial load balance.

Numerical structural analyses of centrifugal compressors operating with CO_2 in a supercritical state.

The current work is part of a project underway in RCGI (Research Centre for Greenhouse Gas Innovation): *Simulation and Optimization of CO2 and CH4 Compressors at Supercritical Conditions.*

CASE STUDIES

Case 1: Centrifugal Compressor operating with air

The first case considered a centrifugal compressor operating with air instead of sCO2. The objective of this study was to structure the process of structural analysis of a centrifugal compressor considering the interaction with aerodynamic loads. The methodology applied was the one-way fluid-structure interaction (FSI), which consists of performing a computational fluid dynamic simulation to predict the pressure field, followed by CFD mesh mapping to the finite element mesh and, finally, the use of these aerodynamic loads as boundary conditions in static structural analysis (Yin et al., 2017), this process is illustrated in Fig. 1.

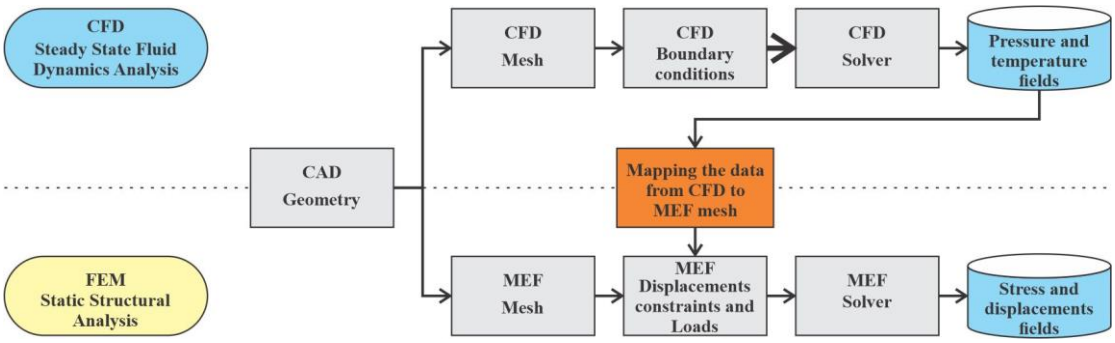

Figure 1 – Procedure of Fluid-Structural Interaction analysis with one-way coupling method.

The geometry of the compressor, Fig. 2a, and the performance data for validation were taken from the papers (Cho et al., 2012; Oh et al., 1997). This compressor is commonly known in the literature as Eckardt's impeller A, due to the original works (Eckardt, 1975; Eckardt, 1976), in which it was studied experimentally. The analysis of CFD was performed considering the cyclic symmetry of the impeller, which allows the use of only one sector, reducing the number of volumes needed for the discretization. The sector was discretized with 465.000 hexahedral elements, Fig. 2b. The working fluid was air as an ideal gas. The boundary conditions used were total pressure and total temperature at the inlet equal to 1,0133 bar and 288,1 K, respectively, and a mass flow rate at the outlet of 5,31 kg/m³, Fig. 2c. The k-e model was used as the turbulence model and the compressor rotational speed was 14.000 RPM.

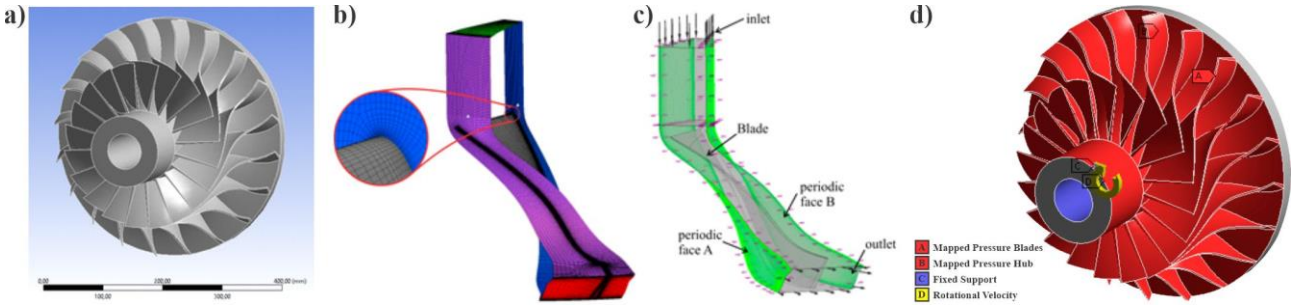

Figure 2 – Eckardt's impeller A. a) CAD geometry; b) CFD sector mesh; c) CFD boundary conditions d) FEM boundary conditions.

About the structural modeling, the material considered was the AL7075, with Young's modulus 71 GPa and Poisson's ratio 0,33. The boundary conditions of the structural analysis are presented in Fig. 2d, where the red surfaces are the mapped pressure application regions, the bore of the impeller were considered fixed (blue surface), and the inertial load generated by the rotational velocity is represented by the yellow arrow.

Both the static structural and modal analyses were made. The stress and displacements levels were evaluated in two different load cases, one with pressure plus the inertial load (LC2), and the other with only the pressure load (LC1). The modal analysis considered the stress stiffening effect that increases the stiffness, due to the displacements and the stress field originated by membrane forces (Cook et al., 2007), which, in the case of centrifugal compressors, are essentially the centrifugal forces. As the extraction of the mode shapes and natural frequencies is an expensive computational task, for the modal analysis cyclic symmetry was also considered. The gyroscopic effects were neglected, due to the model with cyclic symmetry does not allow the use of non-symmetric matrices in the Ansys Mechanical. And the Campbell diagram was generated to help the identification of possible resonance points.

Results of case 1

In Tab. 1, there are comparisons of the results obtained from the CFD analysis against the experimental measurements. The maximum relative error found was 4,30%, less than 5%, validating the prediction process.

Table 1 – Validation of the CFD analysis of the Eckard's Impeller A.

Parameter	CFD analysis	Experimental	Relative error
Isentropic efficiency	0,927	0,889	4,30 %
Pressure ratio	1,87	1,91	1,89 %

With the CFD results validated, the pressure field around the compressor's blades and hub could be extracted. Figure 3a shows the pressure surrounding the blade generated from the CFD simulation. The pressure was used in the structural model by mapping the CFD mesh into the finite element mesh using the triangulation approach (Samareh, 2007).

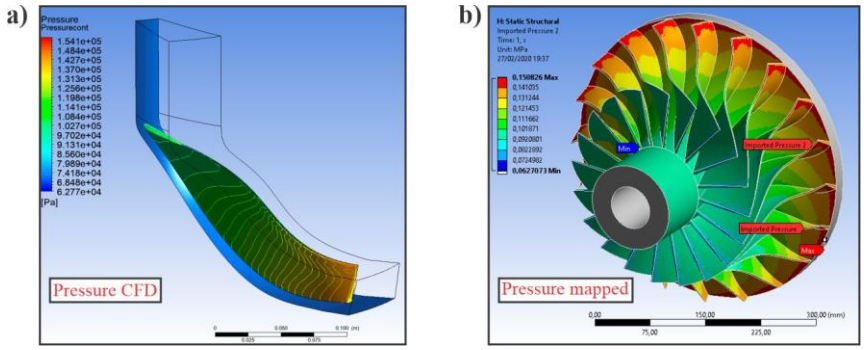

Figure 3 – Pressure field. a) CFD pressure; b) Pressure mapped into the finite element mesh.

The first structural results were obtained through the analysis of a single blade, considering the disk of the impeller as a rigid body, Fig. 4. This kind of analysis has the objective to evaluate if the thickness distribution of the blade is adequate for loads. The maximum values obtained were referent from the LC2, being 0,44 mm the maximum displacements (Fig. 4b), and 134,11 MPa the maximum von Mises stress (Fig. 4d), located near the hub in the trailing edge. Similar results were found in the work of (Cho et al., 2012). When considering only the pressure loads, the values were smaller (Figs. 4a and 4c). As the yield stress of AL7075 alloy is 503 MPa, the stress levels found are safe.

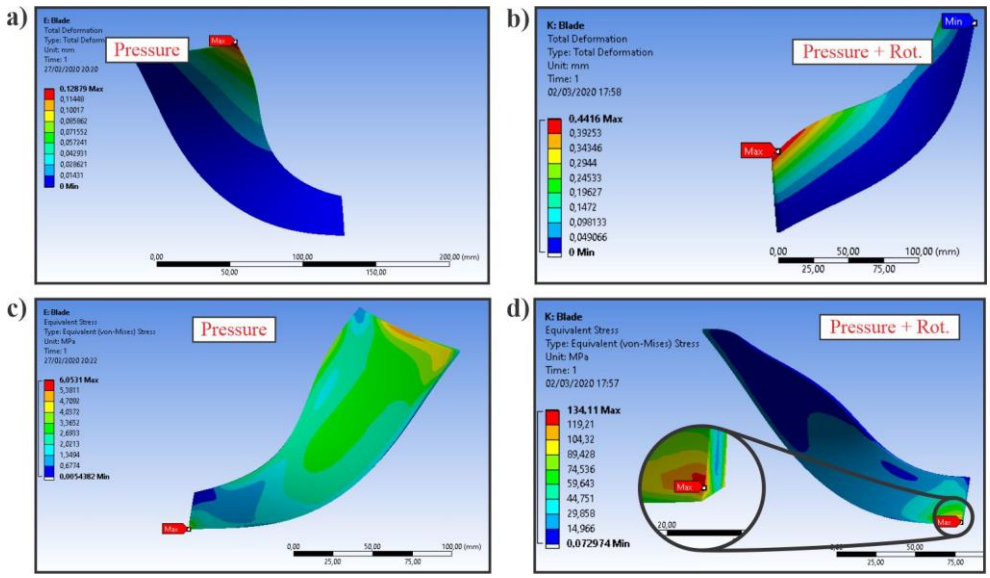

Figure 4 – Single blade structural analysis. a) Displacements of the LC1; b) Displacements of the LC2; c) Stress distribution of the LC1; d) Stress distribution of the LC2.

Then, the next step of the analysis was to consider the disk as a flexible body. The total displacement distributions are shown in Fig. 5. When comparing the values obtained with the single blade model for the LC1, Fig. 4a, about the full impeller model, Fig. 5a, the values found were near, but considering the inertial loads, Fig. 4b and Fig. 5b, the

displacements were from 0,44 mm to 0,60 mm, showing that the flexibility of the disk can not be neglect, even it being stiffer than the blades.

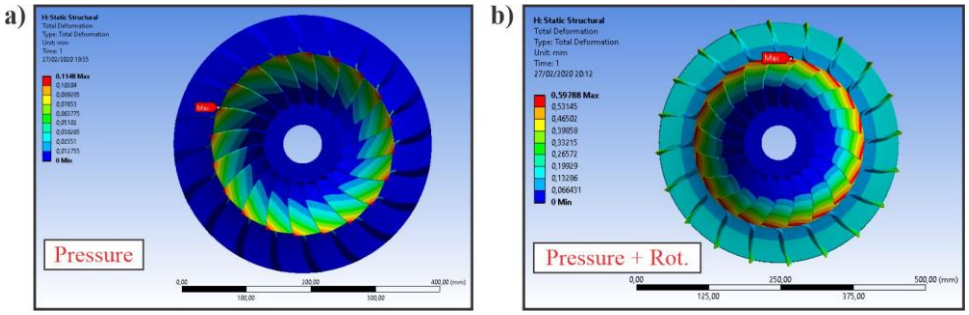

Figure 5 – Impeller structural analysis. a) Displacements of the LC1; b) Displacements of the LC2.

With respect to the stress analysis of the full impeller, the maximum stress value obtained was 238,6 MPa for the LD2, in the bore region, but was also below the yield strength, Fig. 6a. For the case with only the pressure load, the maximum von Mises stress obtained was equal to 5,68 MPa located near the root of the blade in the leading edge, Fig. 6b. Comparing the results with a cracked compressor, Fig. 6c, studied in the work (Chen et al., 2017), it is possible to see that the localization of the maximum and the nucleation of the fatigue failure position are similar. Although the analyses realized were static, pressure fluctuations will occur during compressor operation, even so, this type of analysis is fundamental to identifying stress concentrators that may cause the nucleation of cracks and, consequently, the reduction of the life of the compressor.

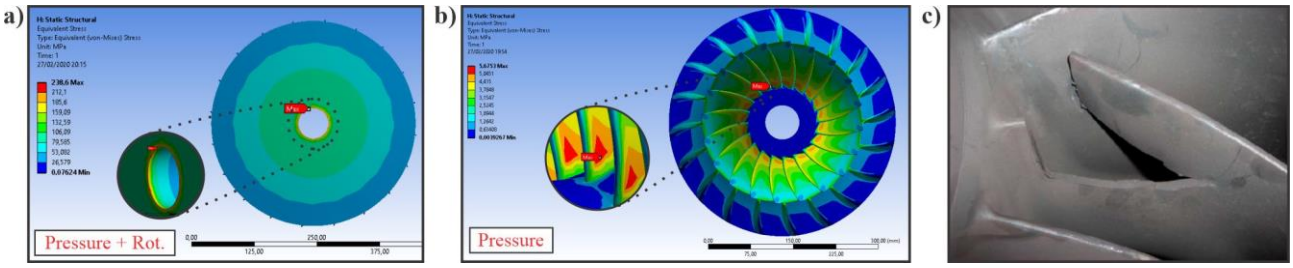

Figure 6 – Impeller structural analysis. a) Stress of the LC2; b) Stress of the LC1; c) Cracked blade.

The modal analysis generated the Campbell diagram presented in Fig. 7. Only the 2, 3, and 4 nodal diameters (ND) modes were calculated, according to (Kushner et al., 2000; Wang et al., 1999), the most worrying modes are those with smaller nodal diameters, due to their greater capacity to transfer energy to the structure. The diagonal dashed lines are the representations of the excitation sources, commonly known as engine orders (EO), that are harmonics of the rotational speed. The line "15EO", for example, is referent to an excitation frequency equal to 15 times the rotation, which can represent fluctuations in the flow generated by the interaction with rotating blades, 15 blades in the case, or even the wakes from inlet-guided vanes, diffusers, nozzles, and others stationary elements. In the diagram, it is possible to see that there are five crossings (red dots) into the $\pm 5\%$ range of the design speed of 14kRPM. These intersections between the natural frequencies and the engine orders are possible resonance points, but it is necessary to investigate the real possibility of resonance, for example, with the generation of the SAFE diagram (Singh et al., 1988), which takes into account not only the frequency coincidence, as well as the shape of the excitation forces.

Case 2: First stage Centrifugal Compressor operating with sCO2

The second case was a centrifugal compressor with application in CCSU. It is the first stage and operates with CO2 in the supercritical state, Fig. 8a. The design speed is 12,5 kRPM, with an inlet pressure of 400 kPa, temperature of 320 K, and 55,56 kg/s mass flow of real gas Carbon Dioxide. The blade geometry was generated using ANSYS Vista CCD and parameterized as shown in Fig. 8b. The CFD analysis was taken in CFX, where the pressure field of the flow was obtained, Fig. 8c. Following the same methodology presented in Fig. 1, the pressure was mapped to the structural finite element model Fig. 8d, which was then analyzed in a static structural analysis, using ANSYS Mechanical.

The chosen material was the 13Cr-4Ni (UNS S42400), based on the work (Dowson et. al., 2008), with a yield strength of 552 MPa (σ_y), the ultimate strength of 689 MPa (σ_u), and Young's modulus 220 GPa. The considered design requirements were defined based on the work (Armand, 1995) and they are as follows:

- Safety factor based on yield strength: $SF_{yd} = 1{,}1 \left(max.stress \leq \frac{\sigma_y}{1{,}1}\right)$;
- Safety factor based on ultimate strength: $SF_{ud} = 1{,}5 \left(max.stress \leq \frac{\sigma_u}{1{,}5}\right)$;
- Safety factor on the maximum stress at 120% speed (burst condition): $SF_{ub} = 0.9\ (max.stress \leq 0.9\sigma_u)$.

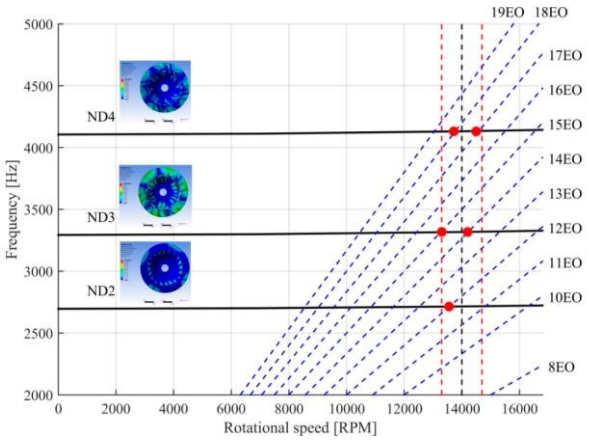

Figure 7 – Campbell diagram of the ND2, ND3, and ND4.

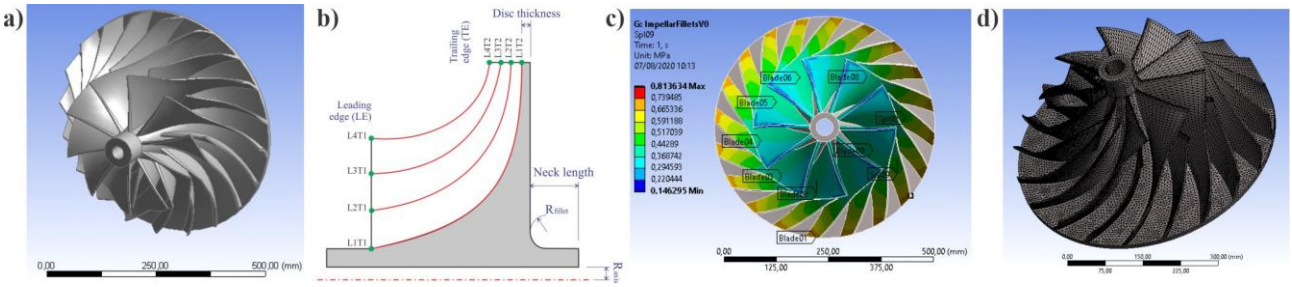

Figure 8 – First case: a) CAD model; b) Parameterization; c) Pressure field; d) Finite element mesh.

The list of the parameters used in the first approach of stress analysis is presented in Tab. 2. The blade thickness distribution was parameterized by the $LxTy$ variables, where $y = 1$ is referent to the leading edge, and $y = 2$ to the trailing edge. About the index x, it indicates the span division of the blades, being 0%, 33%, 66%, and 100%. The other parameters are referent only to the disk geometry, Fig. 8b. The second approach of stress analysis and optimization will be detailed in the following results section.

Table 2 – Parameters values of the baseline and proposed model.

Parameter	Baseline [mm]	Proposed Model [mm]	Parameter	Baseline [mm]	Proposed Model [mm]
L1T1	7,5	8,25	L4T1	3,00	3,30
L1T2	10,00	11,00	L4T2	3,00	2,75
L2T1	6,00	6,60	Rfillet	20,00	20,00
L2T2	7,61	8,43	Raxis	15,00	15,00
L3T1	4,50	4,95	Neck length	60,00	60,00
L3T2	5,32	5,85	Disc thick.	10,00	10,00

Results of case 2

The first stress analysis made obtained the results presented in Tab. 3. As can be seen, the baseline geometry did not reach all the design requirements, the burst criterion was greater than the limit of 0,9. Then, a simplified screening approach was used to obtain a new geometry, which was named as Proposed Model in the Tab. 2. The stress distributions for this new model are shown in Fig. 9a and Fig. 9b, respectively, for the design speed and burst speed conditions, and the maximum von Mises stresses did not exceed the limits, Tab. 3.

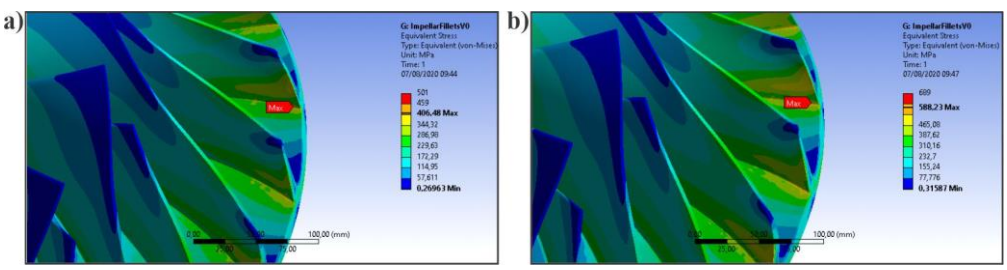

Figure 9 – Von Mises stress of the Proposed Model: a) Design speed of 12,5 kRPM; b) Burst speed of 15 kRPM.

Table 3 – Stress analyses of the baseline and proposed model.

Model	Speed [RPM]	Max. Stress [MPa]	SFyd (>1,1)	SFud (>1,5)	SFub (<0,9)	Pass
Baseline	12500	441	1,25	1,56	-	No
	15000	638	-	-	0,93	
Proposed Model	12500	407	1,36	1,69	-	Yes
	15000	588	-	-	0,81	

Although all criteria are within the requirements for the proposed model, it was necessary to change the thickness of the blades, which can cause a reduction in the aerodynamic efficiency. Then, a metamodel-based optimization (Jiang, P., Zhou, Q., & Shao, X., 2020), was proposed to obtain an optimal geometry with minimum modification on the path flow. The same parameters that are shown in the Tab. 2 were considered, but more two were added, the thickness of the root of the disk and the rear axis radius, as can be seen in Fig. 10a. The fillet radius between the blades and the hub was implemented too, Fig. 10b, totalizing seven parameters.

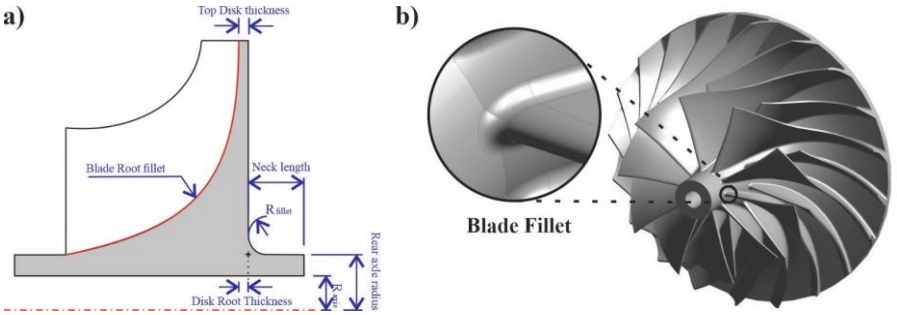

Figure 10 – New parameterization: a) Parameters of the disk; b) Detail of the fillet between the blade and hub.

A design of experiment (DOE) was generated with the Latin Hypercube Sampling (LHS) method, with maximization of the minimum distance of the samples, resulting in a total of 179 points, of which 148 points were extracted to the training of the response surface obtained with the Kriging technique, and the 31 remaining points were used as verification points to determine the error metrics of the model. The quality of the metamodel was evaluated concerning the determination coefficient (R^2), the root mean square error ($RMSE$), the maximum absolute error (MAE) and the maximum relative error (MRE). The values found are presented in Tab. 4. The R^2 and MRE had acceptable values, and despite the RMSE and MAE are greater than the recommended values, 5% and 10%, respectively, due to the necessity of more points in the DOE, they were considered satisfactory.

Table 4 – Metamodel error metrics

R^2	$RMSE$	MAE	MRE
0,94	7,34%	14,98%	4,66%

With the metamodel obtained, a single discipline optimization strategy was conducted. The objective was the minimization of the maximum von Mises stress, and the structural design requirements were used as constraints. The method was the genetic algorithm available in the Ansys DesignXPlorer. The optimal geometry obtained was assessed and compared with the baseline and the results are in Tab. 5. Then, as a conclusion, it was shown that is possible to conduct a structural design preserving the aerodynamic characteristics. This is an important result for cases when it is not possible to perform a multidisciplinary optimization.

Table 5 – Comparison between the baseline and the optimal geometry

Model	RearAxisL [mm]	RootT [mm]	RearAxisR [mm]	FilletDisk [mm]	Raxis [mm]	TopT [mm]	Fillet [mm]	Stress [MPa]	SFyd [-]	SFud [-]	SFub [-]
Baseline	60.00	10.00	35.00	15.00	15.00	10.00	0.00	441.0	1.26	1.57	0.93
Optimal	57.55	24.88	42.41	23.35	15.22	12.08	3.96	398.6	1.38	1.73	0.83

Case 3: Fourth stage Centrifugal Compressor operating with sCO2

As in case 2, the impeller used in this case also works with supercritical CO_2, but this one is the fourth stage, the last of the compressor, Fig. 11a. Due to the lower flow coefficient, the geometry is very different when compared with the first stage, Fig. 8a. Consequently, the pressure levels are higher than those observed in the analysis of case 2, as can be seen in Fig. 11c, that is the pressure field mapped into the finite element mesh, Fig. 11b. The maximum value of the pressure is near 17,55 MPa, about 21 times the obtained in case 2, Fig. 8c. Resulting in much higher deformation and stresses caused by the aerodynamic loads. The material and the design requirements were maintained the same in the structural analysis.

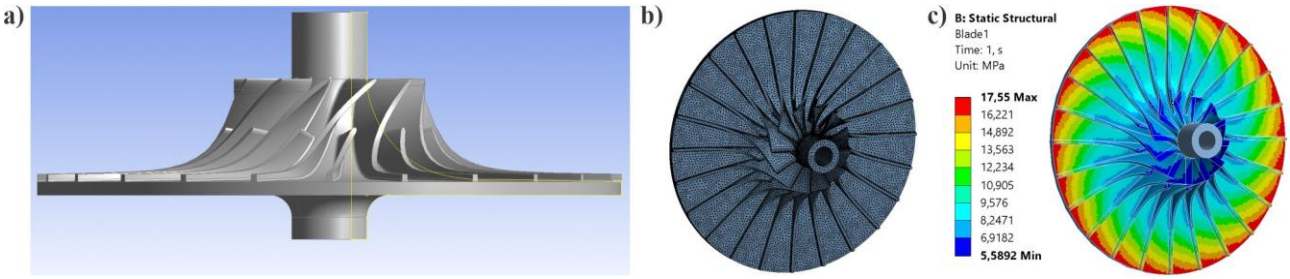

Figure 11 – Fourth stage model: a) CAD model; b) MEF model; c) Pressure mapped.

Due to this higher pressure, the leakage through the gap between the out radius of the impeller and the diffuser generates significant backpressure (Wright et al, 2010), Fig. 12a. In the work (Younsi & Hypolite, 2019), was proposed a model that predicts the pressure distribution in function of the radius of the impeller, Fig. 12b. The model was extrapolated and adapted in this present work as shown in Fig. 12c, where the distribution was partitioned in five regions of the backplate of the disk.

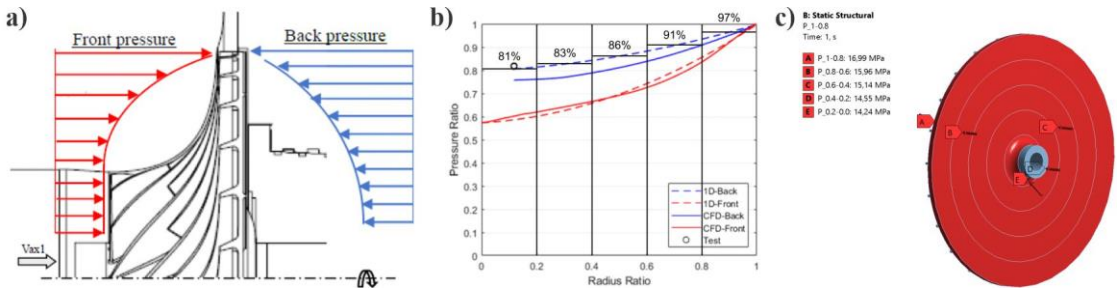

Figure 12 – Backpressure modeling based on the work (Younsi & Hypolite, 2019): a) Front and Backpressure illustration; b) Back pressure in function of the radius; c) Sectioned backpressure.

Results of case 3

The first results, similarly to case 1, were obtained from two loads case, LCA and LCB, in which LCA considers only the centrifugal load, and in LCB is added the pressure load (mapped and back pressures). In Fig. 13a, there is the deformation generated by the inertial load only, when compared with what was obtained in the case with the pressures, Fig. 13b, the total displacements are 8,69 times greater. Differently from what was calculated in case 2, where the pressure loads could be neglected without significantly affecting the static behavior.

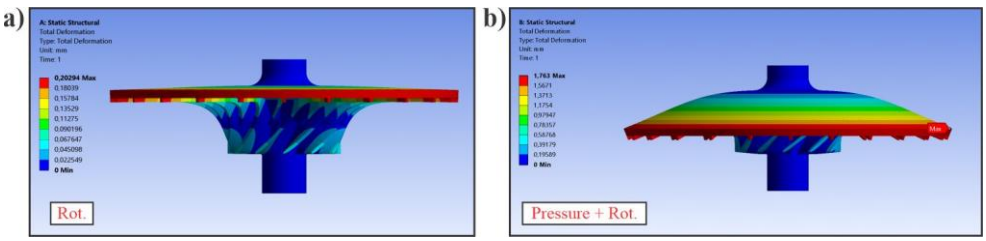

Figure 13 – Baseline displacements: a) Load case LCA; b) Load case LCB (exaggerated for better visualization).

About the stress results, in Figs. 14a and 14b, the distributions of the von Mises stress for the LCA case are presented, the maximum was about 291 MPa, in the backplate near the fillet between the disk and the shaft. However, for the LCB case, the maximum obtained was 1462 MPa, greater than the yield and ultimate tensile strength of the material. Then, following the observed in the DOE analysis of the first stage, a new geometry was proposed for the fourth stage, and as was concluded in that analysis, the flow path was not modified, maintaining the aerodynamic performance of the compressor.

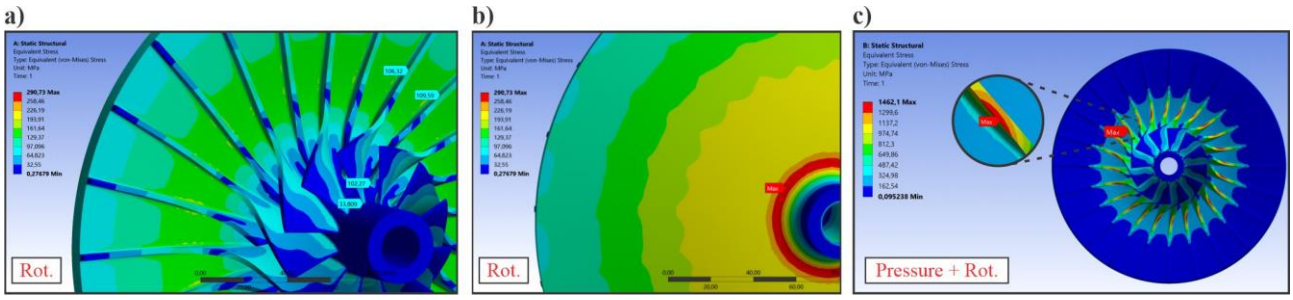

Figure 14 – Baseline stress results: a) Load case LCA front view; b) Load case LCA back view; c) Load case LCB.

The geometry was parameterized as shown in Fig. 15a, the baseline geometry analyzed is presented in Fig. 15b, and the new in Fig. 15c. The comparisons of the geometric parameters are in Tab. 6. As can be seen, the top and root thickness of the disk were increased, as well as the fillet between the backplate and the rear shaft, and the rear axle radius increased too, decreasing the "bending length". The modifications followed the trend of the optimal geometry obtained in case 2 (Tab. 5), and the stress was reduced to levels capable to reach the design requirements.

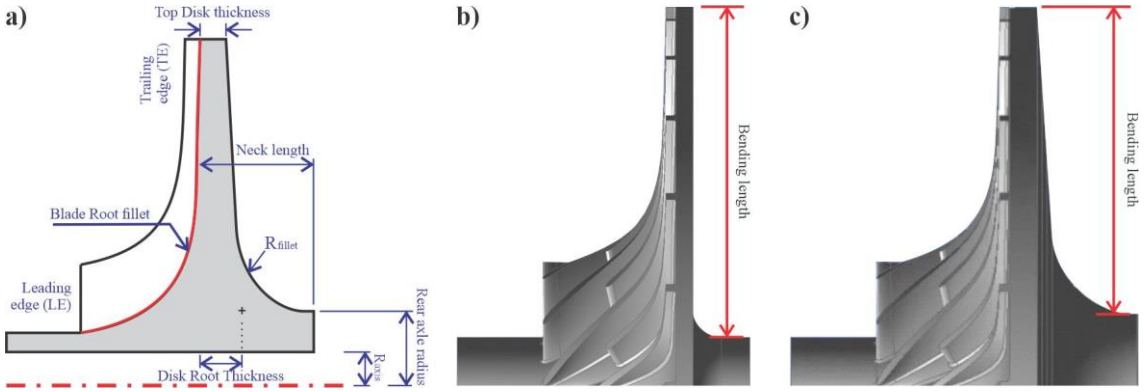

Figure 15 – Fourth stage model: a) Parameterized model; b) Baseline; c) Proposed model.

The plotting of the von Mises stress for the proposed model is in Fig. 16. In Fig. 16a, it was found the maximum value equals to 233MPa, near the root of the splitter and the hub. Now, considering the pressures plus the rotation, Figs. 16b and 16c, the maximum value was 406 MPa in the fillet of the backplate, and the values in the blades were about the values without the pressure load, Fig. 16b. This last observation shows that the axial load generated by the front and the back pressure were almost balanced, reducing the excessive stress found in Fig. 14c for the baseline with the LCB.

Table 6 – Comparison between the baseline and the proposed geometry of the Fourth Stage.

Model	RearAxisL [mm]	RootT [mm]	RearAxisR [mm]	FilletDisk [mm]	Raxis [mm]	TopT [mm]	Fillet [mm]	Stress [MPa]	SFyd [-]	SFud [-]	SFub [-]
Baseline	20.00	6.00	35.00	15.00	10.00	6.00	1.00	1462	0.38	0.47	-
Proposed	45.00	17.00	50.00	30.00	10.00	10.00	1.00	406	1.36	1.70	0.70

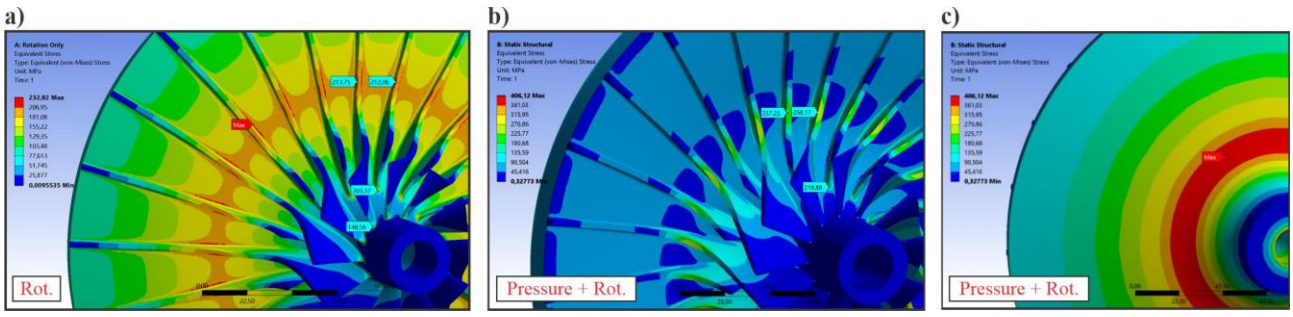

Figure 16 – Proposed model stress results: a) Load case LCA; b) Load case LCB front view; c) Load case LCB.

CONCLUSION

The investigations of the particularities of the structural analyses in each case enabled the achievement of an analysis methodology that will be employed in future works.

In the first case was consolidated the use of the one-way fluid-structural interaction (FSI). Where it was possible to map the pressure field obtained by a CFD to the mesh of the FEM and then verify the influence of the aerodynamic loads in static behavior. The stress and displacement fields for cases with and without pressure load were compared. A Campbell diagram was obtained to help in the identification of possible resonance conditions.

The first stage of the centrifugal compressor with application in CCSU was the second case studied. Three geometries were verified concerning the design requirements. The baseline was not capable to reach all the requirements, then a new geometry was proposed, modifying the thickness distribution. However, changes in the flow path also influence the aerodynamic performance, then a metamodel-based design optimization was conducted, and an optimal geometry without changes in the parameters of the blades was obtained.

The third case studied was the fourth stage of the same compressor. Because of the high-pressure operation in this stage, the influence of the pressure field in the static behavior is higher than observed in the first case. Then simplified modeling of the backpressure load was necessary to balance the axial load. The baseline geometry did not reach the design requirements and a new geometry was proposed following the trends obtained in the metamodel-based design, without modification in the flow path, keeping the aerodynamic efficiency found in separated CFD analysis.

ACKNOWLEDGMENTS

We gratefully acknowledge the support of the RCGI – Research Centre for Gas Innovation, hosted by the University of São Paulo (USP) and sponsored by FAPESP – São Paulo Research Foundation (2014/50279-4 and 2020/15230-5) and Shell Brasil, and the strategic importance of the support given by ANP (Brazil's National Oil, Natural Gas, and Biofuels Agency) through the R&D levy regulation. Also, the support of the UFABC – Federal University of ABC, which provides all the computational and physical infrastructure.

REFERENCES

Armand, S. C. (1995). Structural Optimization Methodology for Rotating Disks of Aircraft Engines. *NASA Technical Memorandum*, *4693*(November), 20.

Baena-Moreno, F. M. et al. (2018). Carbon capture and utilization technologies: a literature review and recent advances. Energy Sources, Part A: Recovery, Utilization, and Environmental Effects, Informa UK Limited, v. 41, n. 12, p. 1403–1433. https://doi.org/10.1080/15567036.2018.1548518.

Chen, X., Xu, S., Wang, X., Ju, W., Yang, S., & Meng, J. (2017). Research on Failure of Semi-Open Centrifugal Impeller Under Aerodynamic Load. *Proceedings of the ASME Turbo Expo 2017: Turbomachinery Technical Conference and Exposition*, *Volume 7B*, 1–11. https://doi.org/10.1115/GT2017-64564.

Cho, S.-Y., Ahn, K.-Y., Lee, Y.-D., & Kim, Y.-C. (2012). Optimal Design of a Centrifugal Compressor Impeller Using Evolutionary Algorithms. *Mathematical Problems in Engineering*, *2012*, 1–22. https://doi.org/10.1155/2012/752931.

Cook, R. D. (2007). Concepts and applications of finite element analysis. John Wiley & sons.

Dowson, P., Bauer, D., & Laney, S. (2008). Selection of Materials and Material Related Processes for Centrifugal Compressors and Steam Turbines in the Oil and Petrochemical Industry. *Proceedings of the 37th Turbomachinery Symposium*, 189–209. https://doi.org/https://doi.org/10.21423/R1SS8C.

Eckardt, D. (1975). Instantaneous measurements in the jet-wake discharge flow of a centrifugal compressor impeller. Journal of Engineering for Power, 97(3), p. 337-345. https://doi.org/10.1115/1.3445999.

Eckardt, D. (1976). Detailed flow investigations within a high-speed centrifugal compressor impeller. Journal of Fluids Engineering, 98(3): 390-39. https://doi.org/10.1115/1.3448334.

Jiang, P., Zhou, Q., & Shao, X. (2020). Surrogate model-based engineering design and optimization. Berlin/Heidelberg, Germany: Springer.

Kushner, F., Richard, S. J., & Strickland, R. A. (2000). Critical Review of Compressor Impeller Vibration Parameters For Failure Prevention. *Proceedings of the 29th Turbomachinery Symposium*.

Oh, H. W., Yoon, E. S., & Chung, M. K. (1997). An optimum set of loss models for performance prediction of centrifugal compressors. *Proceedings of the Institution of Mechanical Engineers, Part A: Journal of Power and Energy*, *211*(4), 331–338. https://doi.org/10.1243/0957650971537231.

Page, B. et al. (2020). The global status of CCS 2020: Vital to achieve net zero. Global CCS Institute.

Samareh, J., 2007. Discrete data transfer technique for fluid-structure interaction. In 18th AIAA Computational Fluid Dynamics Conference (p. 4309).

Saravanamuttoo, H. I. H., Rogers, G. F. C., Cohen, H., Straznicky, P. V., & Nix, A. C. (2017). *Gas Turbine Theory* (7th ed.). Pearson. www.pearson.com/uk

Singh, M. P., Vargo, J. J., Schiffer, D. M., & Dello, J. D. (1988). Safe Diagram - A Design And Reliability Tool For Turbine Blading. *Proceedings of the 17th Turbomachinery Symposium*, 93–102. https://doi.org/10.21423/R1B673.

Umezawa, T. et al. (2020). Statistical characterization of urban CO2 emission signals observed by commercial airliner measurements. Scientific Reports, Springer Science and Business Media LLC, v. 10, n. 1.

Wang, Q., Bartos, J. C., & Houston, R. A. (1999). Methodology of Open Bladed Impeller Resonance Identification. *Proceedings of the 28th Turbomachinery Symposium*, 61–68.

White, M. T., Bianchi, G., Chai, L., Tassou, S. A., & Sayma, A. I. (2020). Review of supercritical CO2 technologies and systems for power generation. *Applied Thermal Engineering*, *185*(December 2020), 28. https://doi.org/10.1016/j.applthermaleng.2020.116447

Wright, S. A., Radel, R. F., Vernon, M. E., Pickard, P. S., & Rochau, G. E. (2010). *Operation and Analysis of a Supercritical CO2 Brayton Cycle*. https://doi.org/10.2172/984129

Yin, T., Pei, J., Yuan, S., Osman, M. K., Wang, J., & Wang, W. (2017). Fluid-structure interaction analysis of an impeller for a high-pressure booster pump for seawater desalination. *Journal of Mechanical Science and Technology*, *31*(11), 5319–5328. https://doi.org/10.1007/s12206-017-1026-z

Younsi, M., & Hypolite, E. (2019). Investigation and prediction models of the axial thrust in centrifugal compressors. *Proceedings of the ASME Turbo Expo*, *2*C-*2019*(June), 0–7. https://doi.org/10.1115/GT2019-90165

RESPONSIBILITY NOTICE

The author(s) is (are) the only party(ies) responsible for the printed material included in this paper.